This paper appears in Journal of Medical Robotics Research, Robotics-Assisted Needle Steering Special Issue, 2018
DOI: 10.1142/S2424905X18420047

Event-triggered 3D Needle Control Using a Reduced-order Computationally Efficient Bicycle Model in a Constrained Optimization Framework

Jay Carriere[a,], Mohsen Khadem[a,], Carlos Rossa[a,], Nawaid Usmani[c,], Ronald Sloboda[c,], Mahdi Tavakoli[a,]

[a] *Department of Electrical and Computer Engineering, University of Alberta, AB, Canada T6G 1H9.*
E-mail: jtcarrie@ualberta.ca (Corresponding Author); mohsen.khadem@ualberta.ca; carlos.rossa@uoit.ca; mahdi.tavakoli@ualberta.ca.

[b] *Cross Cancer Institute and the Department of Oncology, University of Alberta, Edmonton, AB, Canada T6G 1Z2.*
E-mail: ron.sloboda@albertahealthservices.ca; nawaid.usmani@albertahealthservices.ca.

Long flexible needles used in percutaneous procedures such as biopsy and brachytherapy deflect during insertion, thus reducing needle-tip placement accuracy. This paper presents a surgeon-in-the-loop system to automatically steer the needle during manual insertion and compensate for needle deflection using an event-triggered controller. A reduced-order kinematic bicycle model incorporating needle-tip measurement data from ultrasound images is used to determine steering actions required to minimize needle deflection. To this end, an analytic solution to the reduced-order bicycle model, which is shown to be more computationally efficient than a discrete-step implementation of the same model, is derived and utilized for needle-tip trajectory prediction. These needle-tip trajectory predictions are used online to optimize the insertion depths (*event-trigger points*) for steering actions such that needle deflection is minimized. The use of the analytic model and the event-triggered controller also allows for limiting the number and extent of needle rotations (to reduce tissue trauma) in a constrained optimization framework. The system was tested experimentally in three different ex-vivo tissue phantoms with a surgeon-in-the-loop needle insertion device. The proposed needle steering controller was shown to keep the average needle deflection within 0.47 ± 0.21 mm at the final insertion depth of 120 mm.

Keywords: Needle Steering; Event-Trigger Control; Ultrasound Image Guided Surgery.

1. Introduction

Percutaneous procedures have a wide range of clinical applications, including biopsy and brachytherapy. In these procedures, a needle is inserted into tissue and is guided by a clinician towards a desired target location. In the case of biopsy, the goal is to gather tissue samples for diagnostic analysis, and for brachytherapy, the objective is to deposit radioactive seeds for the treatment of cancerous tissues. The diagnostic and therapeutic efficacy of both depends upon the accuracy with which the needle tip is positioned with respect to the target point. This requirement of needle-tip placement accuracy lends itself to the use of robotic assistants that can steer the needle towards the desired target location with high precision.

The therapeutic procedure focused on in this paper is prostate brachytherapy; a procedure whereby long flexible needles, preloaded with radioactive seeds, are inserted through the perineum into the prostate to treat prostate cancer. During the therapy, using both ultrasound-image guidance and a guide template (consisting of a grid of holes), the clinician attempts to steer the needle toward target locations within the prostate where the seeds are then permanently implanted; see Fig. 1 and Fig. 3. This procedure is an attractive treatment option used in early-stage locally-confined prostate cancers [1, 2]. One of the complications in the current clinical practice is that the asymmetric needle-tip bevel causes the needle to deflect during insertion and thus deviate away from the target location, for a recent survey see [3]. This deflection, if uncorrected, both reduces the efficacy of the therapy and increases the side effect profile [4]. With the clinician manually steering the needle, seeds are placed with an average accuracy of 5 mm [5]. This 5 mm error is significant given the 50 mm diameter of the average prostate. Increasing the efficacy of this procedure is of growing practical importance; with a projected prostate cancer diagnosis for one in eight Canadian men in their lifetime [6].

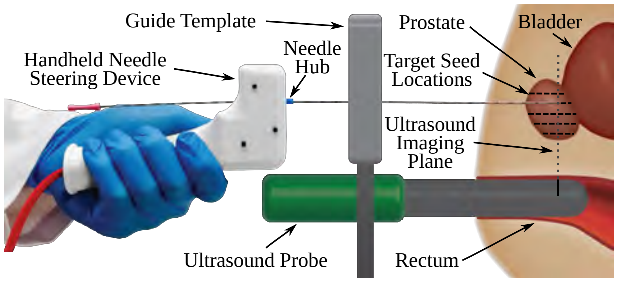

Fig. 1. Standard clinical brachytherapy setup with Transrectal Ultrasound (TRUS) probe, axial imaging plane, hand-held steering device, needle base, and guide template.

This paper presents a semi-autonomous (surgeon-in-the-loop) ultrasound-image-guided system, which can steer the needle during insertion to increase targeting accuracy. The system is designed such that the clinician directly controls the insertion velocity and depth, in this case by inserting the needle attached to a hand-held device (shown in Fig. 1) originally presented in [7]. Real-time ultrasound-image based needle tracking is used to estimate the parameters of a reduced-order nonholonomic kinematic bicycle model. The needle deflection is minimized through the use of an event-triggered control system which optimizes needle rotation during insertion, thus steering the needle. The control system is designed such that, with the addition of the hand-held steering device, it can be incorporated into a standard clinical setup used during prostate brachytherapy without requiring additional sensors or changes to the clinical setup.

The main contribution of this paper is an analytic solution to the reduced-order bicycle model which allows for calculation of the needle-tip trajectory, for the entire needle insertion, without requiring numerical integration. This analytic solution is shown to be more computationally efficient than traditional discrete-step numerical integration methods for needle-tip trajectory calculation and allows the proposed event-triggered control system to reduce needle deflection in real-time.

An overview of related work on ultrasound-image-based needle tracking and control will be given in Sec. 2. A brief overview of the reduced-order bicycle model will be covered in Sec. 3. The event-triggered controller utilizing the analytic solution to the reduced-order kinematic bicycle model along with a detailed comparison of the computational speed of the solution will be shown in Sec. 4. In Sec. 5 the setup used to validate the controller, including the hand-held device, along with results of needle insertion trials in three different tissue phantoms will be presented. Within this section, Sec. 6 covers the algorithm for needle tracking in axial ultrasound images along with the model parameter fitting. The last Sec. 7 gives a discussion of the results obtained along with future challenges to be solved.

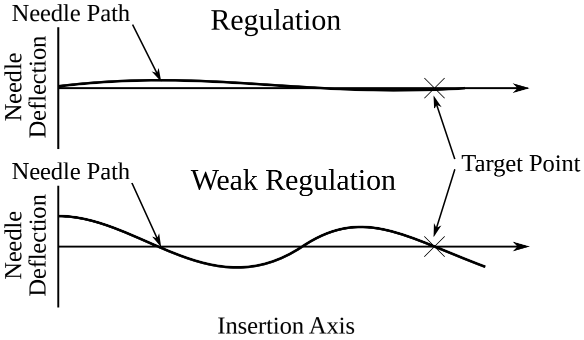

Fig. 2. Comparison of the regulation and weak regulation control paradigms seen in needle steering control, as described in [3].

2. Background

Several different control paradigms have been devised within the context of needle steering for percutaneous procedures, with a thorough review of the control paradigms and their applications given in [3]. One such control paradigm is referred to in the literature as regulation. For regulation, the controller is designed to eliminate needle-tip deflection away from a target axis throughout the entire insertion and is ideal for procedures such as prostate brachytherapy. Another control paradigm is weak-regulation, whereby the needle-tip is only controlled to pass through a desired target point, allowing for larger needle-tip deflection away from the target axis during insertion. Weak regulation is primarily used for procedures such as biopsy but also applicable to brachytherapy. For brachytherapy, weak regulating controllers can be designed to reduce the required number of total needle rotations, and therefore tissue trauma, while maintaining acceptable needle deflection around the target axis. Figure 2 illustrates the difference in deflection minimization between weak-regulation and regulation.

One model used in the literature for the control of long-flexible needles, such as those used in prostate brachytherapy, is known as the kinematic bicycle model. In the context of needle steering, the bicycle model was first presented by [8] and [9] who showed that the 3D trajectory of a beveled needle-tip, during insertion into tissue, is analogous to the trajectory of a bicycle with its front wheel locked at a single angle. This “locked wheel” models the needle trajectory as following a 3D path with a constant radius of curvature (i.e., moving along the edge of a 3D circle) with the direction of curvature related to the angle of the needle-tip bevel. The initial work of [9] used the bicycle model to steer a needle towards a target in a 2D plane. This paper will use a reduced-order bicycle model, originally presented in [10], that will be described in Sec. 3 for control of a needle in 3D.

The kinematic bicycle model, and the underlying constant curvature assumption, has been used in the literature for needle trajectory control in both 2D and 3D scenarios. The work of [11] presented an ultrasound-image-guided needle controller in 2D which merged a mechanical model of needle deflection with the constant curvature constraint for trajectory planning. Through using a local 2D in-plane version of the bicycle model, the researchers [12] and [13] implemented controllers to steer a needle in 3D in the presence of tissue motion. A stochastic controller, modeling tissue through Markov motion uncertainty, was presented by [14] and used the bicycle model and image feedback for needle-tip path planning and steering while allowing for tissue motion. The constant curvature model has also been used in 3D with [15] and [16] fitting parameters of the bicycle model to estimate mechanical needle properties. One minor limitation present in this literature is that the needle path-planning and control requires the kinematic bicycle model to solved through numerical integration, which may require the planning be done in an offline manner. The analytic solution, to be presented in this paper, for a reduced-order version bicycle model is shown to be more computationally efficient than numerical-integration and allows for both path-planning and control to be done in real-time.

Event-triggering is a modern control technique, initially used for distributed control systems, that uses discrete events as a trigger to initiate a control action for both continuous-time and discrete-time systems [17]. Event-triggered control theory presents a cohesive framework to design, and analyze the performance of, aperiodic controllers, where stability of a distributed system can be proven using only knowledge of previous control actions and an estimate of the system state [18]. Using the ideas presented in event-triggered control theory, we will derive an analytic solution to a reduced order bicycle model incorporating discrete changes to the needle rotation velocity (the control output) that are triggered based on inserted needle length (during manual needle insertion by a clinician). One contribution of the controller presented in this paper is that deflection minimization performance can be tuned, through increasing or decreasing the number of event-trigger points, between the weak-regulation and regulation paradigms. The number of event-trigger points is directly related to the total number of needle rotations performed by the controller. Thus, by tuning the number of event-trigger points, tissue trauma can be reduced while keeping the needle-tip deflection during insertion at an acceptable level. The event-triggered presented in this paper can be tuned between regulation type performance, for a procedure such as prostate brachytherapy, or weak-regulation performance, for biopsy procedures.

To minimize the needle-tip deflection during insertion, the event-triggered controller requires an estimate of the initial state of the reduced-order bicycle model. This state estimate will be found by tracking the needle-tip path in ultrasound images. Needle tracking, or segmentation, has been performed in the literature on 3D ultrasound volumes but this paper focuses strictly on needle tracking in 2D images to be more representative of a current clinical setup. In 2D ultrasound images, the needle is typically imaged either in the axial plane, a plane orthogonal to the direction of needle insertion (see Fig. 3), or the sagittal plane, a plane containing the needle and parallel to the direction of needle insertion. In sagittal plane ultrasound images, the needle appears as a distinct white blob or thick curved line, and segmentation can be performed through the use of Gabor Filtering [19] along with the Hough Transform for straight needles [20] and curved needles [21].

In axial plane ultrasound images, (see Fig. 1), it is difficult to distinguish the needle from background noise due to the axial ultrasound image only showing a small cross-section of the needle. Segmentation of the needle in axial plane ultrasound images is, therefore, more challenging than in sagittal plane images. To compensate, axial image segmentation typically combines a needle shape model and a tracking framework, to use information across a series of axial image slices, and measure the needle tip path or position [12, 14, 22]. These tracking algorithms have also been implemented to provide needle tip position feedback for semi-autonomous [23] and fully autonomous needle steering systems [24]. Our work, in [25], used template matching to track the location of the needle tip and used a particle filter to estimate the parameters of a 2D kinematic bicycle model for real-time deflection prediction. This work will use that same image processing technique but will use a genetic algorithm for real-time parameter estimation.

3. Reduced-order kinematic bicycle model

The 5-DoF reduced-order non-holonomic bicycle model used for needle deflection control in this paper was derived in [10] for needle steering based on feedback-linearization using a Frenet-Serret frame. This reduced-order model is similar to the 6-DoF bicycle model commonly seen in the literature [8, 9], but reformulates the system's nonholonomic constraints such that only five states are required fully describe the 3D motion of the needle. At the beginning of needle insertion, a frame attached to the needle tip, $\{T\}$ is coincident with a base frame $\{0\}$. The frame $\{0\}$ is fixed at the point of insertion into tissue; see Fig. 3, with the axes of this frame defined as $[\,^0x',\ ^0y',\ ^0z']$. By convention the position and orientation of the tip-attached frame $\{T\}$, and thus the needle tip, are measured relative to the frame $\{0\}$. The axes of the tip-attached frame $\{T\}$ are labeled $[\,^Tx',\ ^Ty',\ ^Tz']$. The rotation of frame $\{T\}$, about the $^Tz' - {^Ty'} - {^Tx'}$ axes is denoted by the angles ψ, θ, ϕ.

The insertion velocity, $v \in \mathbb{R}$, applied to the base of the needle during insertion translates the tip-attached frame forward along its local $^Tx'$-axis, with the inserted length of the needle defined to be ℓ. The needle tip-path curvature, modeled by a constant κ, forces the tip-attached frame to rotate slowly about its $^Ty'$-axis during insertion, slowly increasing the rotation angle θ, where $\{\theta \in \mathbb{R} : 0 \leq \theta < \pi\}$. The constant κ is defined as the inverse of the radius of curvature of the needle, R, i.e. $\kappa = \frac{1}{R}$, where $\{R \in \mathbb{R} : 0 < R\}$.

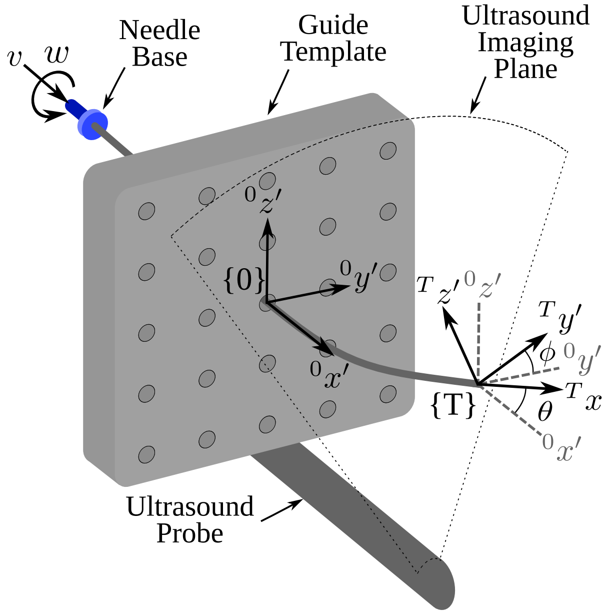

Fig. 3. Coordinate system used for kinematic bicycle model, showing TRUS probe, axial imaging plane, control input and needle base, and guide template.

The needle is modeled as being torsionally stiff; for a given rotational velocity applied to the needle base, $w \in \mathbb{R}$, an equal rotation velocity at the needle tip will be produced about the ${}^Tx'$-axis. The angle of the needle bevel is then equivalent to ϕ, the orientation of the ${}^Ty'$-axis, where $\{\phi \in \mathbb{R} : \pi \leq \phi < \pi\}$. It can be shown that there is no input, or combination of inputs, which can cause rotation about the ${}^Tz'$-axis and so the angle ψ can be removed from the system. The states within the system are then defined as $\dot{X} = [x, y, z, \theta, \phi]$. Readers are urged to look at [10] for further details and proofs of accessibility and controllability of this model.

The original reduced-order model was defined such that the state-space was a differential equation with respect to time and v was explicitly an input. Motivated by [26], the model can be transformed by noting that $v = \frac{d\ell}{dt}$ and thus dividing out the control variable v, resulting in

$$\dot{X} = \begin{bmatrix}\dot{x}\\ \dot{y}\\ \dot{z}\\ \dot{\theta}\\ \dot{\phi}\end{bmatrix} = \begin{bmatrix}\cos(\theta)\\ \sin(\theta)\cos(\phi)\\ \sin(\theta)\sin(\phi)\\ \kappa\\ 0\end{bmatrix} + \begin{bmatrix}0\\0\\0\\0\\1\end{bmatrix} w \qquad (1)$$

where we will now use dot notation to indicate a derivative with respect to needle insertion length ℓ, $\dot{X} = \frac{dX}{d\ell}$. Of note, the control input w is now a rotation velocity with respect to insertion length, $w = \frac{d\phi}{d\ell}$, with units of rad/mm. In this paper, the reduced-order model will be used for control, covered in Sec. 4, with the model parameters found in real-time through ultrasound image processing, discussed in Sec. 6.

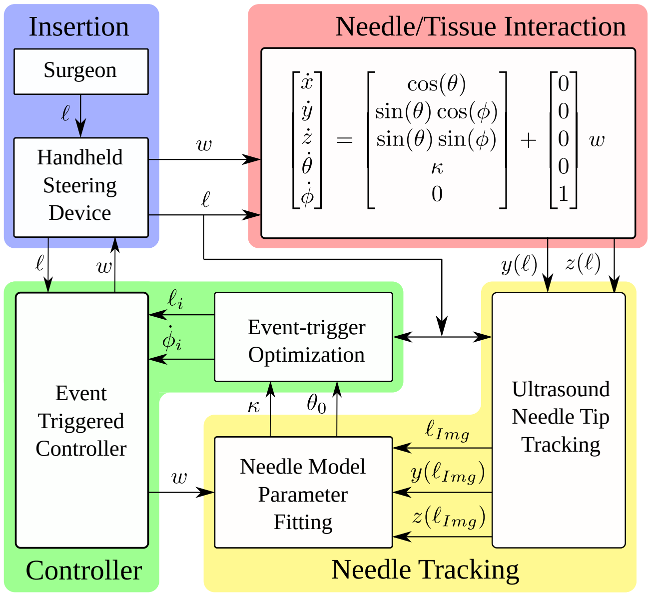

Fig. 4. Control diagram showing semi-autonomous insertion, needle tip tracking in ultrasound images, model fitting, and event-triggered controller.

4. Event-triggered Control

Needle steering in a surgeon-in-the-loop context requires a control algorithm that is both real-time and robust to changes in the needle insertion velocity. This section will present an analytic solution to the 5-DoF reduced order model and the implementation of an event-triggered controller for needle steering. The control loop for the system is diagrammed in Fig. 4. The derived analytic solution of the 5-DoF reduced-order model allows for fast simulation of needle insertion and is ideal in the sense that it does not require a trade-off between numerical accuracy and computational time, as PDE solvers or discrete time-step variants of the kinematic bicycle model typically do.

To implement the 5-DoF bicycle model in a practical control system, while attempting to limit tissue damage, the controller will be designed to reduce needle deflection through slowly varying the needle bevel angle ϕ. Here, in a manner analogous to the clinical practice, the target location is defined to lie at a specified depth on the ${}^0x'$-axis, in line with the direction of insertion. Thus the needle model gives the needle-tip deflection in both the ${}^0y'$ and ${}^0z'$ axes. To solve the closed-loop system equations, based on event-trigger theory, we constrain the output of the controller, ω, such that it only changes once the insertion length of the needle passes the event-trigger point. The method to optimize the locations of the event-trigger points, with respect to insertion length, is given in Sec. 4. For this controller, the number of event-trigger points can be chosen empirically to provide the desired controller performance. Using a small number of event-trigger points will minimize needle rotation velocity at the cost of greater needle-tip deflection away from the ${}^{0}x'$-axis during insertion. Using more event-trigger points will minimize needle-tip deflection during insertion but will require larger needle rotation velocities.

From the state-space representation of the model, in (1), we start by evaluating the differential state equation $\dot{\theta}$ to derive $\theta(\ell)$, noting that this state is independent of the control input $\dot{\phi} = \omega$. The needle insertion depth is denoted by ℓ, with the needle being inserted through the guide template along the ${}^{0}x'$-axis. The initial insertion length is then given as $\ell = 0$ with a desired final insertion length defined as $\ell = \ell_f$, where $\ell_f > 0$. From (1) we can see that $\dot{\kappa} = 0$, thus the solution to this first-order differential equation is

$$\theta(\ell) = \int_0^\ell \dot{\theta}(\ell)\, d\ell = \int_0^\ell \kappa = \kappa\ell\Big|_0^\ell + \theta_0 \tag{2}$$

where θ_0 is the initial value of $\theta(\ell)$ at the point of insertion, i.e. $\theta_0 = \theta(0)$. With the use of the ultrasound image processing the value of θ_0 can be found. Thus, using this, we can find the state of the system $\theta(\ell)$ to be

$$\theta(\ell) = \kappa\ell + \theta_0 \tag{3}$$

where $\{\ell \in \mathbb{R} : 0 \leq \ell \leq \ell_f\}$. With the solution to $\theta(\ell)$ known, the system state $x(\ell)$ can then be found, such that

$$\begin{aligned} x(\ell) &= \int_0^\ell \cos(\theta)\, d\ell = \int_0^\ell \cos(\kappa\ell)\, d\ell \\ x(\ell) &= \frac{\sin(\kappa\ell + \theta_0)}{\kappa}\Big|_0^\ell + x_0 \end{aligned} \tag{4}$$

where, in an identical manner to (3), the limit of integration is the current insertion depth ℓ. From the definition of the base frame $\{0\}$, such that it is located at the initial point of insertion, we have $x(0) \equiv 0$, thus $x_0 = 0$ and $x(\ell)$ is then given as

$$x(\ell) = \frac{\sin(\kappa\ell + \theta_0)}{\kappa} - \frac{\sin(\theta_0)}{\kappa} \tag{5}$$

throughout the insertion interval $0 \leq \ell \leq \ell_f$.

With solutions to both $\theta(\ell)$ and $x(\ell)$ derived, the next step is to solve for $y(\ell)$ and $z(\ell)$. Unlike $\theta(\ell)$ and $x(\ell)$, our control input $\dot{\phi}(\ell)$ clearly effects the response of $y(\ell)$ and $z(\ell)$. To formulate the response of the system using event-trigger control points we consider the total insertion length to be divided into n sections of arbitrary length where, through controller design, $\dot{\phi}(\ell)$ is constant in each section (i.e. use of zero-order hold). Using subscript notation, we will define the space of $l = \{\ell_0 : \ell_1, \ell_1 : \ell_2, ..., \ell_{n-1} : \ell_n\}$. Here $\ell_0 = 0$, and ℓ_n is our target insertion length ℓ_f. We will allow the value of $\dot{\phi}_i$ to change by some finite amount at the event points ℓ_i between each segment. This then defines our event-triggers as these insertion depth points ℓ_i with a corresponding control output after the trigger as $\omega = \dot{\phi}_i$; see Fig. 5.

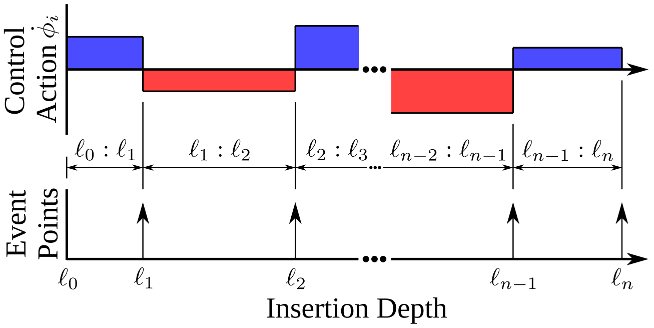

Fig. 5. Event-trigger points partitioning space into sections and zero-order hold on control signal between adjacent points.

The notation used here and throughout the following sections assigns particular meaning to the subscripts used, when used in a function such as $x(\ell)$ it is implied that ℓ can be any value, such that $\ell \in \mathbb{R} : 0 \leq \ell \leq \ell_f$. In contrast, when a subscript is used, such as $\phi(\ell_i)$, this indicates the value of $\phi()$ at the specific depth ℓ_i, with corresponding event-trigger point i. The subscript notion $\dot{\phi}_i$ is used to indicate a control signal value that remains constant after the event point i up until the next event point $i + 1$.

With these definitions, we can evaluate the value of $\phi(\ell)$ for the entire insertion through summation of piece-wise integrals over section, such that

$$\phi(\ell) = \sum_{i=0}^{n-1} f_\phi^i(\ell_i, \ell) + \phi_0 \tag{6}$$

where

$$\begin{aligned} f_\phi^i(\ell_i, \ell) &= \begin{cases} \int_{\ell_i}^{\ell} \dot{\phi}(\ell_i)\, d\ell & \text{if } \ell_i \leqslant \ell < \ell_{i+1} \\ \int_{\ell_i}^{\ell_{i+1}} \dot{\phi}(\ell_i)\, d\ell & \text{if } \ell_{i+1} \leqslant \ell \\ 0 & \text{if } \ell < \ell_i \end{cases} \\ &= \begin{cases} \dot{\phi}(\ell_i) \cdot (\ell - \ell_i) & \text{if } \ell_i \leqslant l < \ell_{i+1} \\ \dot{\phi}(\ell_i) \cdot (\ell_{i+1} - \ell_i) & \text{if } \ell_{i+1} \leqslant \ell \\ 0 & \text{if } \ell < \ell_i \end{cases} \end{aligned} \tag{7}$$

given the initial needle bevel angle of $\phi(0) \equiv \phi_0$.

The solution to $y(\ell)$ is given by

$$y(\ell) = \sum_{i=0}^{n-1} f_y^i(\ell_i, \phi(\ell), \ell) \tag{8}$$

where the piece-wise solution for the needle deflection during each interval, $f_y^i(\ell_i, \phi(\ell), \ell)$, is solved using equation (7) for $\phi(\ell)$ in (10). From the initial placement of frame $\{T\}$ the deflection of the needle at $\ell = 0$ is defined to be zero, such that $y(0) = 0$.

Similarly the corresponding solution to $z(\ell)$ is then

$$z(\ell) = \sum_{i=0}^{n-1} f_z^i(\ell_i, \phi(\ell), \ell) \tag{9}$$

where the piece-wise solution for the needle deflection during each interval, $f_z^i(\ell_i, \phi(\ell), \ell)$, is given in (11) where $z(0) = 0$. Thus, we now have analytic solutions for $y(\ell)$ and $z(\ell)$ giving the deflection of the needle tip over the entire insertion without any need for numerical integration. Using these equations to calculate the needle deflection, the controller will be implemented by optimizing the location of the event-trigger points, i.e. their respective depths, and the value of the zero-order hold rotation velocity after each trigger.

Note in (10) and (11) if $\dot{\phi}(\ell_i) = \pm\kappa$, from the definition in (7), it indicates that $\phi(\ell) = \kappa\ell + \phi(\ell_i)$ in the region $\ell_i \leqslant \ell < \ell_{i+1}$ such that one of the terms $\kappa\ell + \theta_0 \pm \phi(\ell)$ will reduce to $\theta_0 \pm \phi(\ell_i)$. Thus the corresponding sin() or cos() function will be a constant over that interval. Being as $\dot{\phi}_i$ is the control output the optimization routine can also be constrained such that $\dot{\phi}(\ell_i) \neq \pm\kappa$.

4.1. *Insertion simulation computational performance*

As stated, one of the advantages of the analytic solution is its reduced computational complexity when compared to the discrete step simulation of the reduced-order kinematic bicycle model. Due to the nonholonomic constraints in the system and the single control input ω, the needle-tip cannot move in an arbitrary direction. If given a set

$$\begin{aligned}
f_y^i(\ell_i, \phi(\ell), \ell) &= \begin{cases} \int_{\ell_i}^{\ell} \sin(\theta(\ell))\cos(\phi(\ell))\, d\ell & \text{if } \ell_i \leqslant \ell < \ell_{i+1} \\ \int_{\ell_i}^{\ell_{i+1}} \sin(\theta(\ell))\cos(\phi(\ell))\, d\ell & \text{if } \ell_{i+1} \leqslant \ell \\ 0 & \text{if } \ell < \ell_i \end{cases} \\
&= \begin{cases} \displaystyle\int_{\ell_i}^{\ell} \frac{\sin(\theta(\ell)+\phi(\ell)) + \sin(\theta(\ell)-\phi(\ell))}{2}\, d\ell & \text{if } \ell_i \leqslant \ell < \ell_{i+1} \\ \displaystyle\int_{\ell_i}^{\ell_{i+1}} \frac{\sin(\theta(\ell)+\phi(\ell)) + \sin(\theta(\ell)-\phi(\ell))}{2}\, d\ell & \text{if } \ell_{i+1} \leqslant \ell \\ 0 & \text{if } \ell < \ell_i \end{cases} \\
&= \begin{cases} -\dfrac{1}{2}\left(\dfrac{\cos(\kappa\ell+\theta_0+\phi(\ell))}{\kappa+\dot{\phi}(\ell_i)} + \dfrac{\cos(\kappa\ell+\theta_0-\phi(\ell))}{\kappa-\dot{\phi}(\ell_i)}\right)\Bigg|_{\ell_i}^{\ell} & \text{if } \ell_i \leqslant \ell < \ell_{i+1} \\ -\dfrac{1}{2}\left(\dfrac{\cos(\kappa\ell+\theta_0+\phi(\ell))}{\kappa+\dot{\phi}(\ell_i)} + \dfrac{\cos(\kappa\ell+\theta_0-\phi(\ell))}{\kappa-\dot{\phi}(\ell_i)}\right)\Bigg|_{\ell_i}^{\ell_{i+1}} & \text{if } \ell_{i+1} \leqslant \ell \\ 0 & \text{if } \ell < \ell_i \end{cases}
\end{aligned} \tag{10}$$

$$\begin{aligned}
f_z^i(\ell_i, \phi(\ell), \ell) &= \begin{cases} \int_{\ell_i}^{\ell} \sin(\theta(\ell))\sin(\phi(\ell))\, d\ell & \text{if } \ell_i \leqslant \ell < \ell_{i+1} \\ \int_{\ell_i}^{\ell_{i+1}} \sin(\theta(\ell))\sin(\phi(\ell))\, d\ell & \text{if } \ell_{i+1} \leqslant \ell \\ 0 & \text{if } \ell < \ell_i \end{cases} \\
&= \begin{cases} \displaystyle\int_{\ell_i}^{\ell} \frac{\cos(\theta(\ell)+\phi(\ell)) - \cos(\theta(\ell)-\phi(\ell))}{2}\, d\ell & \text{if } \ell_i \leqslant \ell < \ell_{i+1} \\ \displaystyle\int_{\ell_i}^{\ell_{i+1}} \frac{\cos(\theta(\ell)+\phi(\ell)) - \cos(\theta(\ell)-\phi(\ell))}{2}\, d\ell & \text{if } \ell_{i+1} \leqslant \ell \\ 0 & \text{if } \ell < \ell_i \end{cases} \\
&= \begin{cases} \dfrac{1}{2}\left(\dfrac{\sin(\kappa\ell+\theta_0+\phi(\ell))}{\kappa+\dot{\phi}(\ell_i)} - \dfrac{\sin(\kappa\ell+\theta_0-\phi(\ell))}{\kappa-\dot{\phi}(\ell_i)}\right)\Bigg|_{\ell_i}^{\ell} & \text{if } \ell_i \leqslant \ell < \ell_{i+1} \\ \dfrac{1}{2}\left(\dfrac{\sin(\kappa\ell+\theta_0-\phi(\ell))}{\kappa+\dot{\phi}(\ell_i)} - \dfrac{\sin(\kappa\ell+\theta_0-\phi(\ell))}{\kappa-\dot{\phi}(\ell_i)}\right)\Bigg|_{\ell_i}^{\ell_{i+1}} & \text{if } \ell_{i+1} \leqslant \ell \\ 0 & \text{if } \ell < \ell_i \end{cases}
\end{aligned} \tag{11}$$

of control actions, for instance, the event-triggering points and rotation values, then the needle-tip position throughout insertion can be found through simulation. The inverse operation, finding the control actions that will lead to the needle-tip passing through a desired point or set of points, is not straightforward and requires the use of an optimization routine, like the one covered in Sec. 4.2. In general, these optimization routines simulate the insertion process many times while modifying the control actions taken during insertion to find a set of control actions which result in a needle-tip path that passes through the target point(s). In the context of needle steering, where the target location is located at the final insertion depth, then the entire insertion must then be simulated which can have a significant computational cost. This section will give a brief overview of how the reduced-order model can be simulated versus the event-triggered model. For both of these methods, the number of computational steps will be shown and a theoretical performance comparison will be made.

Normally, to simulate a needle insertion using the reduced-order formulation of the needle model, given in (1), the Euler method is used to solve the state-space differential equation at each time step via the discrete-step form of the equation $X_{K+1} = X_K + \frac{\partial}{\partial x} f(X_K)\Delta\ell + \omega_K$. Here K is the discrete-step depth during the simulation and w_K is the control action per step, where $\omega_K = \omega\Delta\ell$. This expansion results in the following discrete system

$$X_{K+1} = \begin{bmatrix} x_K \\ y_K \\ z_K \\ \theta_K \\ \phi_K \end{bmatrix} + \begin{bmatrix} \cos(\theta_K) \\ \sin(\theta_K)\cos(\phi_K) \\ \sin(\theta_K)\sin(\phi_K) \\ \kappa \\ 0 \end{bmatrix} \Delta\ell + \begin{bmatrix} 0 \\ 0 \\ 0 \\ 0 \\ 1 \end{bmatrix} w_K \quad (12)$$

where the state within the system X_K consists of the values of $X_K = [x_K, y_K, z_K, \theta_K, \phi_K]$ at the discrete insertion depth K. To evaluate the computational cost of both the discrete-time reduced-order model and the analytic solution used for the event-triggered model the cost of each simulation step will be found. For both algorithms, the step-wise computational cost is defined to be the number of mathematical operations required, defined as n_{calc}. These algorithms will calculate the needle tip deflection at a desired final insertion depth. Here, we define mathematical operations to be the functions cos(), sin(), add(), sub(), mul(), div() and will ignore any computations with respect to the loop counters. As an example, in line 4 of Alg. 4.1, the calculation $y_{K+1} \leftarrow \sin(\theta_K) \cdot \cos(\phi_K) \cdot \Delta\ell + y_K$ would be computed as $y_{K+1} = \mathrm{add}(y_K, \mathrm{mul}(\Delta\ell, \mathrm{mul}(\sin(\theta_K), \cos(\phi_K))))$ requiring 5 calculations, thus $n_{calc} = 5$ as indicated.

For the discrete-step reduced-order model, each step updates the states of the system model using the Euler method above (12). Starting at the initial simulation step, $K = 0$, the initial state of the system is defined as $X_0 = [x_0, y_0, z_0, \theta_0, \phi_0]$. The simulation proceeds until the desired final insertion step calculated, defining the last time simulation step to be K_{end}. The algorithm for simulating the discrete-time needle can then be described as follows, with the symbols ' · ' and ' / ' used to indicate multiplication and division respectively.

Algorithm 4.1. Discrete-time step simulation

```
Require: $X_0, \Delta\ell, \omega_k, \kappa$
1: $K = 0$
2: while $K < K_{end}$ do
3:     $x_{K+1} \leftarrow \cos(\theta_K) \cdot \Delta\ell + x_K$                          ▷ $n_{calc} = 3$
4:     $y_{K+1} \leftarrow \sin(\theta_K) \cdot \cos(\phi_K) \cdot \Delta\ell + y_K$        ▷ $n_{calc} = 5$
5:     $z_{K+1} \leftarrow \sin(\theta_K) \cdot \sin(\phi_K) \cdot \Delta\ell + z_K$        ▷ $n_{calc} = 5$
6:     $\theta_{K+1} \leftarrow \kappa \cdot \Delta\ell + \theta_K$                         ▷ $n_{calc} = 2$
7:     $\phi_{K+1} \leftarrow \phi_K + \omega_K$                                            ▷ $n_{calc} = 2$
8:     $K \leftarrow K + 1$
```

From inspection, the computation cost of each simulation step K is $n_{calc} = 17$. Assuming the simulation consists of d simulation steps discretized along the insertion depth a total computational complexity of $n_{calc} = 17d$ will result, which grows linearly with the number of insertion steps to be simulated.

The analytic solution for the event-triggered needle model allows for a computational speed increase for insertion simulation. Using the results of equations (10) and (11) we can simulate the entire needle insertion in a more efficient manner. The model can be evaluated by calculating the changes to the needle state at the insertion depths corresponding to the chosen number of event points, n including the initial and final insertion depths, defined above as l_0 and l_n. As above, our control signal ω is held constant between event-trigger points giving a zero-order hold for $\dot{\phi}(\ell_i)$.

For brevity, we will define the state of the needle to be $X_i = [x_i, y_i, z_i, \theta_i, \phi_i]$ at a depth ℓ_i corresponding to the event-trigger point i. At the depth of each event-trigger point, ℓ_i, the rotation speed and direction of the needle are changed; here we indicate the velocity after the event point as $\dot{\phi}_i$. Again we used subscript notation from Sec 4, where we defined our space ℓ to be broken into sections, such that $\ell = \{\ell_0 : \ell_1, \ell_1 : \ell_2, ..., \ell_{n-1} : \ell_n\}$. The initial state of the needle, at the point of insertion, is then defined as $X_0 = [x_0, y_0, z_0, \theta_0, \phi_0]$. The final insertion state of the needle is denoted as $X_n = [x_n, y_n, z_n, \theta_n, \phi_n]$. The algorithm for simulating the needle is then the following.

Algorithm 4.2. Event-triggered needle simulation

```
Require: $X_0, \dot{\phi}_i, \kappa$
$i = 0$
while $i < n$ do
    $\theta_{i+1} \leftarrow \kappa \cdot \ell_{i+1} + \theta_i$    ▷ $n_{calc} = 2$
    $\phi_{i+1} \leftarrow \phi_i + \dot{\phi}_i \cdot (l_{i+1} - l_i)$    ▷ $n_{calc} = 3$
    $x_{i+1} \leftarrow (\sin(\theta_{i+1}) - \sin(\theta_0))/\kappa$    ▷ $n_{calc} = 4$

    Steps to calculate $y_{\ell_{i+1}}$
    $y_{p1} \leftarrow \cos(\theta_i + \phi_i)/(\kappa + \dot{\phi}_i)$    ▷ $n_{calc} = 4$
    $y_{p2} \leftarrow \cos(\theta_i - \phi_i)/(\kappa - \dot{\phi}_i)$    ▷ $n_{calc} = 4$
    $y_{p3} \leftarrow \cos(\theta_{i+1} + \phi_{i+1})/(\kappa + \dot{\phi}_{i+1})$    ▷ $n_{calc} = 4$
    $y_{p4} \leftarrow \cos(\theta_{i+1} - \phi_{i+1})/(\kappa - \dot{\phi}_{i+1})$    ▷ $n_{calc} = 4$
    $y_{i+1} \leftarrow (-y_{p3} - y_{p4} + y_{p1} + y_{p2})/2$    ▷ $n_{calc} = 4$

    Steps to calculate $z_{\ell_{i+1}}$
    $z_{p1} \leftarrow \sin(\theta_i + \phi_i)/(\kappa + \dot{\phi}_i)$    ▷ $n_{calc} = 4$
    $z_{p2} \leftarrow \sin(\theta_i - \phi_i)/(\kappa - \dot{\phi}_i)$    ▷ $n_{calc} = 4$
    $z_{p3} \leftarrow \sin(\theta_{i+1} + \phi_{i+1})/(\kappa + \dot{\phi}_{i+1})$    ▷ $n_{calc} = 4$
    $z_{p4} \leftarrow \sin(\theta_{i+1} - \phi_{i+1})/(\kappa - \dot{\phi}_{i+1})$    ▷ $n_{calc} = 4$
    $z_{i+1} \leftarrow (z_{p3} + z_{p4} - z_{p1} - z_{p2})/2$    ▷ $n_{calc} = 4$
    $\ell \leftarrow \ell + 1$
```

For each event point, we then have a computational cost of $n_{calc} = 49$ for calculating the deflection in both the y and z axis. For an insertion to a length ℓ_n, where there are $n - 1$ control actions taken, there will be a total of n steps to calculate, thus the computational complexity is then $n_{calc} = 49(n)$ which also grows linearly, but with respect to the number of rotations only. Even though the per-event computation cost is higher, simulating a small number of rotations during the insertion will be at least an order of magnitude smaller that than the cost of simulating the discrete-time system.

One of the primary disadvantages is that the discrete-time simulation accuracy is dependent on the number of steps used, with accuracy increasing with the number of steps. Empirically, the insertion depth must be discredited into steps of 0.5 mm or smaller to result in a reasonable simulation accuracy at the final insertion depth, such that the 120 mm insertion depth used in this paper requires 241 or more simulation steps. For the implementation of the controller used in Sec. 6.2, for 3 event-triggered rotations, the analytic solution has an absolute cost of 196 operations whereas the discrete-time step solution would require 4097 math operations to fully simulate each insertion. The analytic event-mode algorithm allows a full 17 simulations to be run in the same amount of time as a single insertion simulation through the discrete-time step method. This computational speed up implies that the control algorithms built on this analytic solution can be implemented in real-time even in low-end hardware. In addition, the analytic solution does not use any approximation of the underlying differential equations and therefore, offers optimal accuracy without requiring additional simulation points, providing one of the contributions of this paper.

4.2. *Event-triggered control optimization*

The analytic solution of the reduced-order kinematic model facilitates the development of an online optimization routine for the event-triggered controller. This routine will be designed to achieve the stated goal of both minimizing needle deflection and total number of needle rotations. Minimizing needle deflection will be achieved through optimizing the location of event-trigger points, along $\dot{\phi}(\ell)$, and associated changes in needle rotation velocity at those points. With the target location defined to be on the ${}^0x'$-axis, parallel to the direction of needle insertion, needle deflection will be defined as the Euclidean distance

$$e(\ell) = \sqrt{y(\ell)^2 + z(\ell)^2} \tag{13}$$

for a particular insertion depth ℓ. With this definition of needle deflection, a cost function used for minimizing needle deflection can be given as

$$\mathcal{L} = \min\left(\alpha\sqrt{y(\ell_f)^2 + z(\ell_f)^2} + \beta \max\left(\sqrt{y(\ell)^2 + z(\ell)^2}\right)\right) \tag{14}$$

where α and β are weighting constants and $\max(\sqrt{y(\ell)^2 + z(\ell)^2})$ represents the maximum deflection during insertion, $\ell \in \{0 : \ell_f\}$. This allows the controller to be tuned from weak regulation, where $\alpha > 0$ and $\beta = 0$, towards the deflection minimization performance of a regulating controller when $\alpha = 0$ and $\beta > 0$. The controller can also implement a weighted minimization of both objectives when $\alpha, \beta > 0$.

With the needle steering control actions being performed through event-triggering, the online optimization is implemented through finding event points, ℓ_i, along with the required change in needle rotation velocity, $\Delta\dot{\phi}_i$, at those points which minimize the cost. For this controller implementation, the number of event points must be chosen before the insertion. This results in a segmentation of the insertion space $\ell = \{\ell_0 : \ell_1, \ell_1 : \ell_2, ..., \ell_{n-1} : \ell_n\}$ with each segment having a desired needle base rotation velocity $\omega = \dot{\phi}(\ell_i)$, where $\{i \in 0, 1, ..., n-1\}$. As a first step in optimization, the result given in (7) is rearranged to limit the total change of the value of $\phi(\ell)$ in each segment. This change in $\phi(\ell)$ in each segment is limited by a constant $\Delta\dot{\phi}_i$, and is used in

$$|\phi(\dot{\ell_i})| \leqslant \frac{(\ell_{i+1} - \ell_i)}{\Delta\dot{\phi}_i} \text{ where } \ell_i \leqslant \ell < \ell_{i+1} \tag{15}$$

so that the value of $\dot{\phi}_i$ for each segment can be limited.

Using (15) allows tissue trauma to be limited by a choice of $\Delta\dot{\phi}_i$ independently of the needle deflection cost function. For this paper, the value of $\Delta\phi_i$ was empirically chosen to be π, such that the total number of rotations is directly limited to be equal or less than half of the number of event points chosen. Using this limit, the cost function minimization now is independent of any tissue effects for a given number of event-trigger points.

The minimization of the cost function is done by a genetic algorithm [27]. Here a traditional genetic algorithm was modified to have performance closer to simulated annealing by implementing a large number of cross-overs and large uniform random distribution used to seed each generation. The algorithm was "greedy" in that it returned only the single best-performing individual which was then propagated and compared and crossed-over with new individuals created from the uniform distribution. The two needle model parameters, found through ultrasound imaging, θ_0 and κ were updated at the beginning of each iteration. The number of individuals tested at each iteration was held constant, and the number of cross-over individuals created was chosen to be equal to the number of regular individuals.

Each individual consisted of C_i coupled event-trigger points and control signal values $< \ell_i, \dot{\phi}_i >$, where $i = 1, 2...C_i$ to describe the control actions for a complete insertion, the cross-overs were made by swapping a random number of coupled values between two individuals. The cross-over and random individual generator were constrained such that the algorithm only optimized control actions which could be taken in the future as the needle is inserted deeper into tissue. To do this, the values of $< \ell_i, \dot{\phi}_i >$ from the best individual of the previous generation were used for any point i where the current insertion depth was greater than ℓ_i. The result from the simulation of each individual was multiplied by α and stored, as the simulation returns the needle-tip deflection at the target insertion depth, $\sqrt{y(\ell_f)^2 + z(\ell_f)^2}$, and incorporates the minimal rotation constraint.

To calculate the second component of the cost function $\beta \max \left(\sqrt{y(\ell)^2 + z(\ell)^2} \right)$, each pair of adjacent trigger-points in the individual were used to check if the values of $\dot{y}(\ell)$ or $\dot{z}(\ell)$, defined in (1), had crossed zero in that section. This zero crossing implies the needle deflection was at a maximum or minima. The values of $y(\ell)$ and $z(\ell)$ at the points where $\dot{y}(\ell)$ or $\dot{z}(\ell)$ are equal to zero were evaluated by inserting the depth, ℓ, where the derivatives are zero into equations (10) and (11). The largest result of $\sqrt{y(\ell)^2 + z(\ell)^2}$ across all of the zero-crossing points was multiplied by β and used to cacluate that individual's score with respect to the cost function, if there was no zero-crossing in $\dot{y}(\ell)$ or $\dot{z}(\ell)$ then the largest deflection is the final-tip deflection, and this was multiplied by β and used instead. The average computation time of the controller optimization routine during the insertion experiments is given in Table 3 where each generation of the genetic algorithm consisted of 60 individuals, 30 of which were created through cross-overs.

5. Experimental Setup

During the experiments, ultrasound images are captured and processed in real-time to return the needle deflection. The ultrasound transducer, see Fig. 8, was mounted on a motorized linear rail which moved the transducer such that the needle-tip was always contained in the imaging plane. The ultrasound machine used for the experiments was an Ultrasonix Touch with a 4DL14-5/38 Linear 4D transducer (Ultrasonix Corp, Richmond, BC, Canada). For these experiments, only the 2D imaging functionality of the ultrasound probe was used. The needle was controlled during insertion using a hand-held steering device, Fig 8, originally developed in [7]. Optical tracking markers were placed on the hand-held device and a Micron Tracker (HX60 from Claron Technology Inc., Toronto, ON, Canada) was used to measure the length of the needle inserted into tissue. For the phantom tissue insertions, the needles used were standard 18-gauge 200 mm prostate seeding needles (Eckert & Ziegler BEBIG GmbH, Berlin, Germany). The image processing, controller optimization, and event-triggered controller were all programmed in Matlab 2016a (The Mathworks Inc, Natwick, MA, USA) and ran using the Simulink Real-Time environment, on an Intel Core i7-3930K running at 3.20 GHz (Intel Corporation, Santa Clara, CA, USA).

6. Ultrasound Image Processing

For each of the insertion experiments, 2D ultrasound image slices are processed in real-time at a frame-rate of 20 Hz. The 2D functionality of the probe, rather than 3D/4D functionality, was used to replicate the imaging capabilities of the transrectal ultrasound probes (TRUS) used clinically. As shown in Fig. 8, during needle insertion the ultrasound probe is translated along the direction of needle insertion, the ${}^0x'$-axis, such that the needle tip is always captured in the ultrasound image slice. These ultrasound images are processed in real-time using an altered version of the algorithm presented in [25] to track the needle-tip deflection. The images are captured at discrete time intervals, corresponding to the 20 Hz frame rate of the ultrasound machine, with the imaging time step denoted by k_{US}. With the ultrasound probe is moving along the ${}^0x'$-axis, the image frame, corresponding to the ${}^0y'$ and ${}^0z'$ axes, captures the needle tip deflection (with respect to the target ${}^0x'$-axis). The pixel coordinates of the image are indicated by py and pz and the pixel intensity of the image, at time step k_{US}, is defined as $I_{k_{US}}(py, pz)$. The insertion depth of the needle was also measured for each of the ultrasound images, defined as $\ell_{k_{US}}$, and this information is used along with the tracked needle-tip location to fit parameters of the reduced-order bicycle model, to be covered in Sec. 6.1. The image processing routine for each frame consists of two stages which are shown in Fig. 6. The first stage is a preprocessing stage that enhances the visibility of the needle tip to make it more distinct from the tissue background in the image and to make the tracking invariant to changes in the needle tip pixel intensity. The second stage uses template matching to perform the needle tip tracking. At the beginning of insertion, a user clicks on the needle tip in the first frame of the ultrasound image and the image enhancement and tracking are done using a region-of-interest (ROI) around this point.

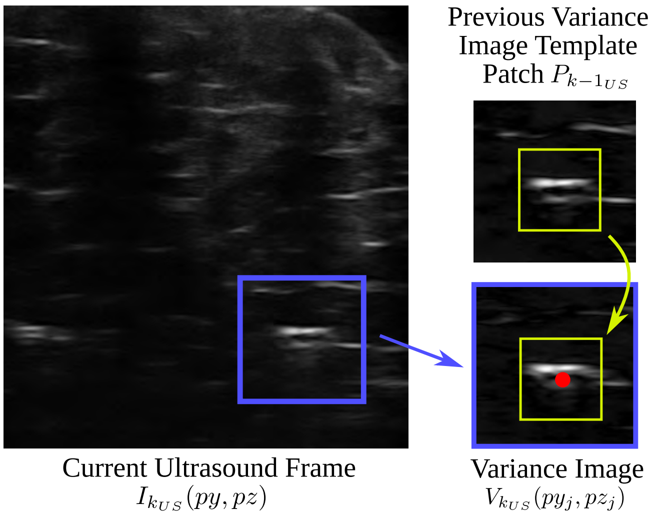

Fig. 6. Ultrasound image processing showing original input image, variance image, template patch, and resulting needle-tip location (indicated by red dot).

For preprocessing, the needle-tip visibility is improved by the creation of a variance image of the ROI. This variance image, when used for tracking, is similar in theory to the sum of conditional variance method presented in [28]. To calculate the variance image, statistics of the pixel intensity in the ROI are used, given

$$\begin{aligned} \mu_{k_{US}} &= \frac{1}{n_{px}} \sum_{j=1}^{n_{px}} I_{k_{US}}(py_j, pz_j) \\ \sigma_{k_{US}} &= \frac{1}{n_{px}} \sqrt{\sum_{j=1}^{n_{px}} \left(I_{k_{US}}(py_j, pz_j) - \mu_{k_{US}}\right)^2} \end{aligned} \tag{16}$$

where n_{px} is the number of pixels in the ROI, py_j and pz_j are the pixel locations within the ROI, $\mu_{k_{US}}$ and $\sigma_{k_{US}}$ are the resulting mean and standard deviation of the pixel intensities. The variance image is then calculated as

$$V_{k_{US}}(py_j, pz_j) = \frac{|I_{k_{US}}(py_j, pz_j) - \mu_{k_{US}}|}{\sigma_{k_{US}}} \tag{17}$$

where $V_{k_{US}}$ is the resulting variance image intensity for each pixel py_j, pz_j in the ROI. This results in an increase of contrast between the needle and the background tissue.

To perform the needle tip tracking, a method similar to [29] is used, under the assumption that the needle-tip location only changes by a small amount between subsequent ultrasound images due to the mechanical characteristics of the needle. Needle tip tracking is done using sum-absolute-difference template matching between a small patch of the variance image in the previous frame, $P_{k-1_{US}} \subset V_{k-1_{US}}(py_j, pz_j)$, centered around the needle tip, py_{TIP} and pz_{TIP}, and the region of interest in the current frame $V_{k_{US}}(py_j, pz_j)$. Due to the use of variance images, this sum-absolute-difference template matching is equivalent to preforming normalized cross-correlation based template matching. The center position of the best template match is the needle-tip position, $py_{TIP|k_{US}}$ and $pz_{TIP|k_{US}}$, which is converted into a metric deflection, in mm, in the ${}^0y'$ and ${}^0z'$ axis. The metric needle tip deflections for each image frame are denoted by $y_{US}(\ell_{k_{US}})$ and $z_{US}(\ell k_{US})$, where the pixel-to-millimeter ratios were measured experimentally with a ratio 0.10 $\frac{\text{mm}}{\text{px}}$ for the ${}^0y'$-axis and 0.12 $\frac{\text{mm}}{\text{px}}$ for the ${}^0z'$-axis. The tracked needle tip is then used for estimation of θ_0 and κ during the needle insertion. For the experimental results, presented in Sec. 6.2 with the image processing time given in Table. 3, the size of the region-of-interest was a 129px×129px square and the size of the needle-tip template was 65px×65px.

6.1. *Image based parameter fitting*

Two of the parameters of the reduced-order bicycle, θ_0 and κ are required for the event-trigger control optimization. These parameters correspond to the initial angle of needle insertion and the (inverse of) the radius of curvature. The ultrasound processing algorithm returns the location of the needle tip and the corresponding insertion depth, resulting in the $\ell_{k_{US}}, y_{US}(\ell_{k_{US}}), z_{US}(\ell_{k_{US}})$ in metric coordinates. During insertion, the location of the needle-tip is recorded for every frame, and once the needle has been inserted past a depth of 10 mm, the values of θ_0 and κ are estimated, with an updated estimate returned with every frame. Here the value of 10 mm was chosen empirically to allow for a small amount of needle deflection to occur before estimation such that the value of κ can be measured. Note that the values of θ_0 and κ are defined to remain constant for a single insertion but may change from insertion to insertion. During insertion, as the parameter estimates are updated, the current best estimate is used in the controller optimization routine. The controller optimization routine simulates the needle insertion using previous control actions (if any event-trigger depths have been passed) on the current system estimate, thus keeping θ_0 and κ constant for that insertion simulation. The simulation of the needle parameter fitting algorithm, given at the end of this section, shows that the estimate settles to the correct values very quickly, within 40 mm of needle insertion, so in practice, the model parameters being used for control optimization remain essentially constant after that depth.

As with the optimization for the event triggered controller, the parameter fitting for the model was done using a modified genetic algorithm. The same percentage of cross-overs and generation of random individuals to refill the population per iteration were used. The contrast to the control optimization algorithm, this algorithm the best 30% of the population was propagated forward at each iteration. Another difference was the way that the individuals were constructed, each individual consisted only of a single set of coupled values $< \tilde{\theta}_0, \tilde{\kappa} >$. Due the limit on $\theta(\ell)$ in the model, $\{\theta \in \mathbb{R} : 0 \leq \theta < \pi\}$, and the use of the guide template during insertion which mechanically constrains the needle during insertion into tissue such that θ_0 is small, the value of $\tilde{\theta_0}$ was limited in the algorithm to the range 0 rad $\leq \tilde{\theta_0} \leq$ 0.174 rad (0.174 rad $\approx 10°$). The value of $\tilde{\kappa}$ was also constrained to the range $\frac{1}{10000} \leq \tilde{\kappa} \leq \frac{1}{500}$ which is larger range than required from data gathered from previous insertion experiments and the literature. To solve for these parameters, the needle path is simulated for a the set of initial values $< \tilde{\theta_0}, \tilde{\kappa} >$ resulting in deflections $\tilde{y}(\ell)$ and $\tilde{z}(\ell)$. The best individual is chosen such that it minimizes the following cost function

$$\mathcal{L}_{Fit} = \min_{<\tilde{\theta_0},\tilde{\kappa}>} \sum_{j=1}^{n} \frac{\sqrt{\left[\tilde{y}(\ell_j) - y_{US}(\ell_j)\right]^2 + \left[\tilde{z}(\ell_j) - z_{US}(\ell_j)\right]^2}}{n} \tag{18}$$

where the score $\mathcal{L}_{Fit}$ is minimized simulated needle tip path is closest to the observed tip path at measurement test points $j = 1, 2, ..., n$. Multiple measurement points j are used, rather than just the current needle-tip location, to make the parameter estimation routine more robust to image noise and occlusion based needle-tip localization errors, which occur intermittently during needle-tip tracking. For this implementation, these points were chosen to measure the needle location a equidistant insertion depths spanning from the insertion point, $\ell = 0$, to the current needle-tip point ℓ_{Img}. For the experimental results 11 test points were empirically determined to be sufficient for parameter fitting. To convert from $\ell_{k_{US}}$ to $x(\ell_{k_{US}})$, (4) was inverted using each individual's $\tilde{\kappa}$. Finally, for each incoming frame an iteration of the genetic algorithm as run, where the system was simulated using the analytic solution given in Sec. 4, incorporating the control actions that had been taken up to the current insertion depth. The L_{Fit} was evaluated using the resulting needle-tip path from simulation and the measured needle-tip locations from the frames closest to each j test point depth. The $< \tilde{\theta_0}, \tilde{\kappa} >$ of the best performing individual was returned as the values θ_0 and κ used for the control optimization. The computation time of the parameter estimation routine is given in Table. 3 where 50 individuals were used for each generation.

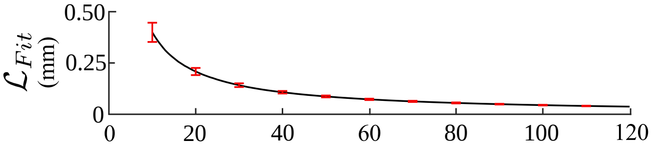

Fig. 7. Needle parameter estimitation score with respect to insertion depth.

The needle parameter optimization was validated in simulation by comparing the needle-tip path of a simulated insertion with known $< \theta_0, \kappa >$ values to the needle-tip path predicted with the estimated parameters $< \tilde{\theta_0}, \tilde{\kappa} >$ from the genetic algorithm. For the validation, 10000 insertion were simulated with uniformly random selections of θ_0 and κ_0, where the value of θ_0 was tested in the range $0 \leq \theta_0 \leq \frac{\pi}{4}$ and κ was tested in the range $\frac{1}{10000} \leq \kappa \leq \frac{1}{500}$. To simulate a "measured" needle-tip path, zero-mean Gaussian noise was added to the simulated needle deflection (derived from equations (10) and (11), such that $y_{US}(\ell) = y(\ell) + N$ and $z_{US}(\ell) = z(\ell) + N$ with $N \sim \mathcal{N}(0, 0.5)$. The parameters $< \tilde{\theta_0}, \tilde{\kappa} >$ were estimated using simulated values with ℓ being incremented in 1.0 mm steps. The plot of the average estimator score, $\mathcal{L}_{Fit}$, is given in Fig. 7 with the error bars showing the standard deviation of the estimator score across the 10000 simulations. These results show that the parameter fitting is able to estimate the needle shape with an mean-squared error of 0.1 mm after the needle has been inserted to a depth of 40 mm.

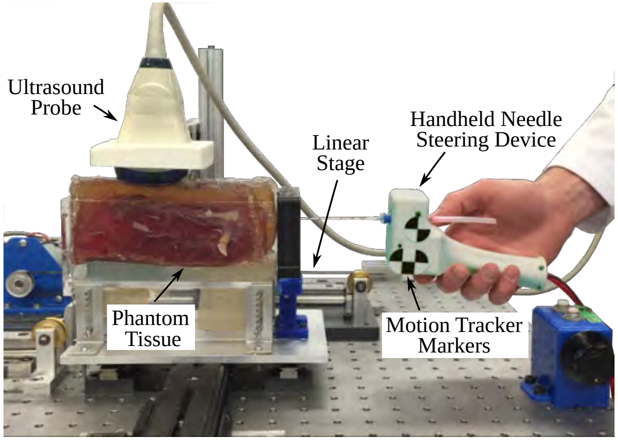

Fig. 8. Experimental setup with ultrasound probe, hand-held needle insertion device, and tissue phantom.

6.2. *Experimental Results*

Three different tissue phantoms were fabricated to evaluate the performance of the needle steering system. Two non-homogeneous tissue phantoms were made from bovine and porcine tissue embedded in gelatin (Knox from Kraft Inc., Northfield, IL, USA). These bovine and porcine phantoms were created to closely resemble the ultrasound imaging and mechanical properties of human tissue. The gelatin was used to hold the tissue in the experimental setup and to provide a flat surface for the ultrasound probe to scan along, such that there was sufficient contact between the probe and the tissue phantom to maintain ultrasound image quality throughout the insertion (see Fig. 8). A third tissue phantom made entirely from plastisol (M-F Manufacturing Co, Fort Worth, USA) which has friction and stiffness properties higher than seen in human tissue. The elevated friction and stiffness create a more challenging scenario for the controller as the needle deflection during insertion is increased.

A total of 10 insertion trials was performed for each of the three phantom tissues, with each insertion having a desired target depth of 120 mm. The needle base rotation was performed by the hand-held device using the optimal event-trigger points and rotation values found in by the genetic algorithm. The optimization parameters, α and β, were chosen to be 10 and 1 respectively. For these results, only three event-trigger points were used and the number of total needle rotations was limited to be less than 3. For most of the trials, the optimized event-triggered control output resulted in fewer than two full rotations. The needle insertion length, ℓ, required for the controller and ultrasound image processing was measured in real-time using the micron device; see Fig. 8.

The deflection of the needle tip away from the ${}^0x'$-axis was measured through ultrasound imaging. The needle tip location at the target insertion depth was used to evaluate the performance of the controller. As in equation (14), the Final Tip Deflection is calculated as

$$\text{Final Tip Deflection} = \sqrt{y(\ell_f)^2 + z(\ell_f)^2} \tag{19}$$

where ℓ_f represents the target insertion depth. The controller was tuned to minimize deflection over the entire insertion. To evaluate this, the other performance measure that was used was the Mean Tip Deflection, given by

$$\text{Mean Tip Deflection} = \int_{\ell=0}^{\ell_f} \frac{\sqrt{y(\ell)^2 + z(\ell)^2}}{\ell_f} d\ell \tag{20}$$

which calculates the average needle tip deflection away from the ${}^0x'$-axis throughout the insertion. The last metric that was evaluated was the total rotation amount that the needle made. To calculate this, the absolute of each control action $\dot{\phi}_i$ was taken and the resulting value of $\phi(\ell)$ evaluated, where the initial bevel angle, ϕ_0, is neglected. This simplified to the following

$$\text{Total Rotation Amount} = |\phi(\ell_f)| = \sum_{i=0}^{n-1} \left| f_\phi^i(\ell_i, \ell_f) \right| \tag{21}$$

where $f_\phi^i(\ell_i, \ell)$ is evaluated using the method in (7). The values for the Final Tip Deflection and Mean Tip Deflection, and Total Rotation Amount were averaged over the results for the 10 insertions per tissue phantom in Table 1. Maxiumum Total Rotation Amount and maximum Tip Deflection at any length during insertion are given in Table 2. The needle tip-path captured for the porcine, bovine, and plastisol phantoms are displayed in Fig. 9a, Fig. 9b, Fig. 9c respectively. The computational time of the image processing algorithm, the parameter estimation algorithm, and the control optimization algorithm are presented in Table 2 with the template patch sizes and number of individuals per generation given in Sec. 6, Sec. 6.1, and Sec. 4.1 respectively.

Table 1. Average Needle Insertion Results

Phantom Tissue	Final Tip Deflection Average (mm)	Mean Tip Deflection Average (mm)	Total Rotation Amount (degrees)
Porcine	0.40 ± 0.24	0.25 ± 0.06	174 ± 86
Bovine	0.51 ± 0.14	0.31 ± 0.08	177 ± 84
Plastisol	0.48 ± 0.25	0.30 ± 0.12	137 ± 68

Table 2. Maximum Needle Insertion Results

Phantom Tissue	Max Final Tip Deflection Average (mm)	Max Total Rotation Amount (degrees)
Porcine	0.86	306
Bovine	0.69	306
Plastisol	0.90	242

Table 3. Processing Time per Image Frame

Procedure	Average Time (ms)	Max Time (ms)
Image Processing	36.0 ± 0.4	40.0
Parameter Estimation	1.6 ± 0.7	6.3
Control Optimization	4.6 ± 1.9	8.16

From the tabular data, the controller is shown to perform approximately the same across the three tissue types. The Final Tip Defection average across all 30 trials was 0.47 mm with an averaged Mean Tip Deflection of 0.27 mm. The maximum needle tip deflection at the target was 0.90 mm, which compares favorably to the literature surveyed in [3] and greatly exceeds the current clinical accuracy demonstrated in [5].

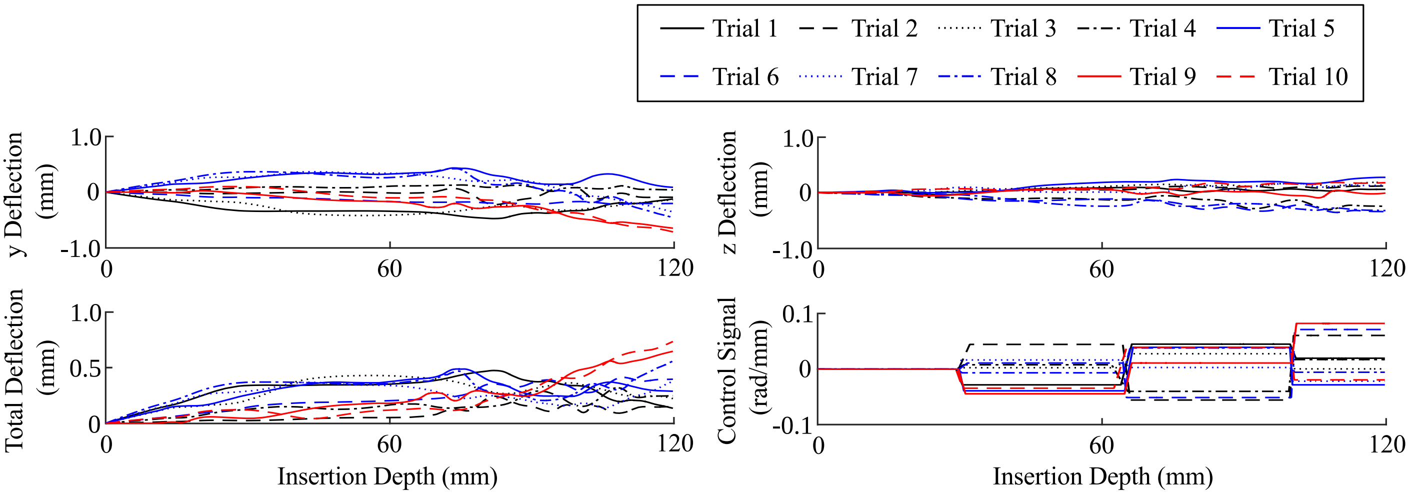

(a) Needle tip path and control signal in porcine tissue.

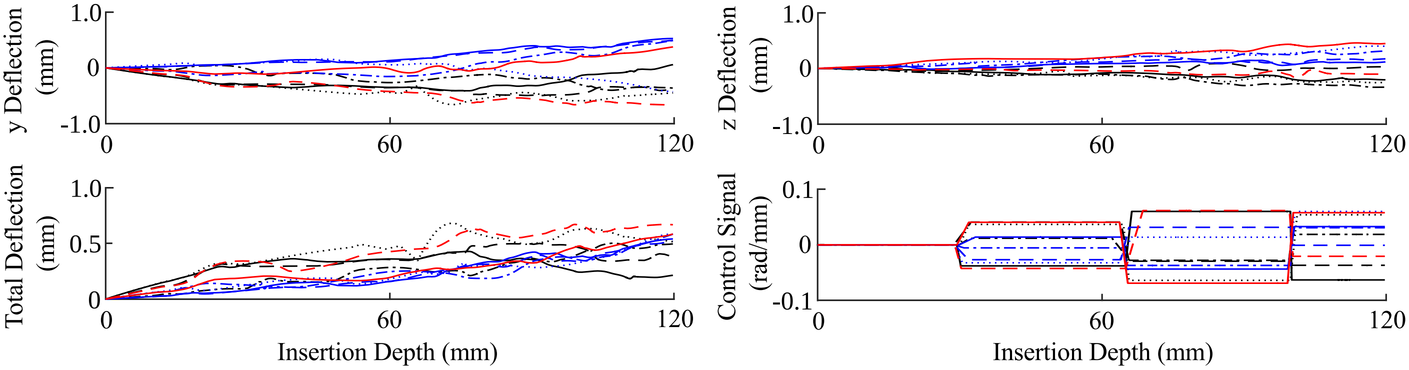

(b) Needle tip path and control signal in bovine tissue.

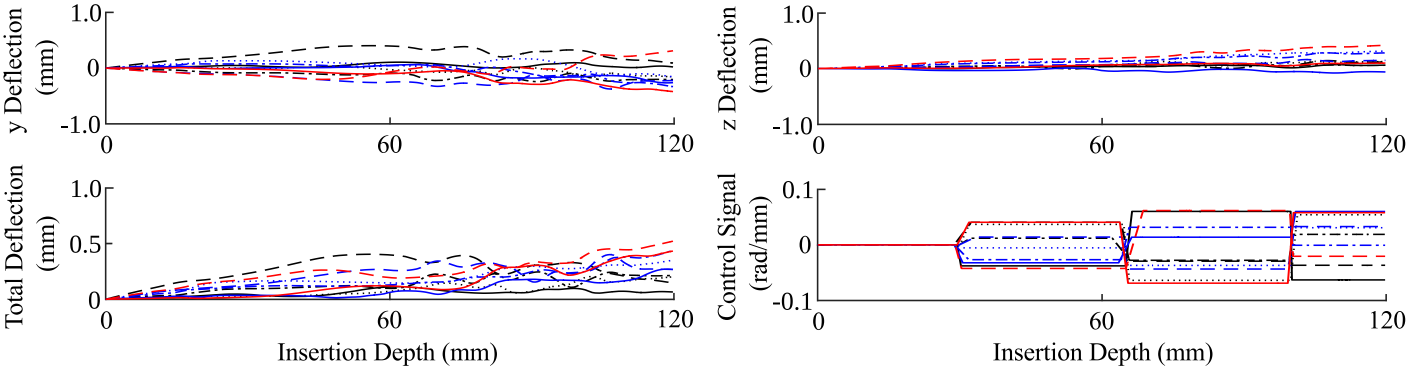

(c) Needle tip path and control signal in plastisol tissue.

Fig. 9. Experimental results for three different tissue phantoms.

7. Conclusion

We have demonstrated a system designed for use in either biopsy or brachytherapy percutaneous procedures. This system steers the needle using a hand-held device using an event-trigger based controller designed to reduce needle deflection during insertion. The controller incorporates a nonholonomic reduced-order bicycle model with required model parameters being estimated online from ultrasound images. The parameter estimation and control signal planning use the presented solution to the kinematic bicycle model which is shown to increase model simulation performance by 21x when compared to a discrete-time step implementation of the model. From insertion trials in ex-vivo tissue phantoms, the controller is shown to decrease Final Tip Deflection to an average of 0.47 mm and Mean Tip Deflection to an average of 0.27 mm, significantly better than seen clinically at current. The total amount of needle rotation was constrained during insertion with the maximum total needle rotation of 306^o during experimentation.

Future work will involve the application of the analytic bicycle model solution in other control paradigms. In particular, the model can be used for intraoperative path planning to steer the needle around obstacles and towards targets located away from the insertion axis. Future work could also involve changes to model parameter fitting, by incorporating uncertainty directly into the analytic model through a Bayesian statistic or Markov chain approach.

Acknowledgments

This work was supported by the Natural Sciences and Engineering Research Council (NSERC) of Canada under grant CHRP 446520, the Canadian Institutes of Health Research (CIHR) under grant CPG 127768, and by the Alberta Innovates - Health Solutions (AIHS) under grant CRIO 201201232.

References

[1] L. Potters, C. Morgenstern, E. Calugaru, P. Fearn, A. Jassal, J. Presser and E. Mullen, Adult urology: Oncology: Prostate/testis/penis/urethra: 12-year outcomes following permanent prostate brachytherapy in patients with clinically localized prostate cancer., *The Journal of Urology* **173** (2005) 1562 – 1566.

[2] D. Bowes and J. Crook, A critical analysis of the long-term impact of brachytherapy for prostate cancer: a review of the recent literature., *Current Opinion in Urology* **21**(3) (2011) 219 – 224.

[3] C. Rossa and M. Tavakoli, Issues in closed-loop needle steering, *Control Engineering Practice* **62** (2017) 55 – 69.

[4] J. E. Dawson, T. Wu, T. Roy, J. Y. Gu and H. Kim, Dose effects of seeds placement deviations from pre-planned positions in ultrasound guided prostate implants., *Radiotherapy And Oncology: Journal Of The European Society For Therapeutic Radiology And Oncology* **32**(3) (1994) 268 – 270.

[5] M. F. Jamaluddin, S. Ghosh, M. P. Waine, R. S. Sloboda, M. Tavakoli, J. Amanie, A. D. Murtha, D. Yee and N. Usmani, Quantifying ^{125}I placement accuracy in prostate brachytherapy using postimplant transrectal ultrasound images, *Brachytherapy* **16**(2) (2017) 306 – 312.

[6] Canadian Cancer Society's Steering Committee, Canadian Cancer Statistics, Available: http://www.cancer.ca/statistics. (2015).

[7] C. Rossa, N. Usmani, R. Sloboda and M. Tavakoli, A hand-held assistant for semiautomated percutaneous needle steering, *IEEE Transactions on Biomedical Engineering* **64** (March 2017) 637–648.

[8] W. Park, J. S. Kim, Y. Zhou, N. J. Cowan, A. M. Okamura and G. S. Chirikjian, Diffusion-based motion planning for a nonholonomic flexible needle model, *Proceedings of the 2005 IEEE International Conference on Robotics and Automation*, (April 2005), pp. 4600–4605.

[9] R. J. Webster, J. S. Kim, N. J. Cowan, G. S. Chirikjian and A. M. Okamura, Nonholonomic modeling of needle steering, *The International Journal of Robotics Research* **25**(5-6) (2006) 509–525.

[10] M. Khadem, C. Rossa, N. Usmani, R. Sloboda and M. Tavakoli, Feedback-linearization-based 3D needle steering in a frenet-serret frame using a reduced order bicycle model *2017 American Control Conference (ACC)* **In press** (2017).

[11] N. Abolhassani, R. Patel and F. Ayazi, Needle control along desired tracks in robotic prostate brachytherapy, *Systems, Man and Cybernetics, 2007. ISIC. IEEE International Conference on*, (Oct 2007), pp. 3361–3366.

[12] G. J. Vrooijink, M. Abayazid, S. Patil, R. Alterovitz and S. Misra, Needle path planning and steering in a three-dimensional non-static environment using two-dimensional ultrasound images, *The International Journal of Robotics Research* **33**(10) (2014) 1361–1374.

[13] S. Patil, J. Burgner, R. J. Webster and R. Alterovitz, Needle steering in 3-D via rapid replanning, *IEEE Transactions on Robotics* **30** (Aug 2014) 853–864.

[14] R. Alterovitz, M. Branicky and K. Goldberg, Motion planning under uncertainty for image-guided medical needle steering, *The International Journal of Robotics Research* **27**(11-12) (2008) 1361–1374.

[15] S. Misra, K. Reed, B. Schafer, K. Ramesh and A. Okamura, Mechanics of flexible needles robotically steered through soft tissue., *International Journal of Robotics Research* **29**(13) (2010) 1640 – 1660.

[16] P. Moreira and S. Misra, Biomechanics-based curvature estimation for ultrasound-guided flexible needle steering in biological tissues, *Annals of Biomedical Engineering* **43**(8) (2015) 1716–1726.

[17] P. Tabuada, Event-triggered real-time scheduling of stabilizing control tasks, *IEEE Transactions on Automatic Control* **52** (Sept 2007) 1680–1685.

[18] W. P. M. H. Heemels, K. H. Johansson and P. Tabuada, An introduction to event-triggered and self-triggered control, *2012 IEEE 51st IEEE Conference on Decision and Control (CDC)*, (Dec 2012), pp. 3270–3285.

[19] M. Kaya and O. Bebek, Needle localization using gabor filtering in 2D ultrasound images, *Robotics and Automation (ICRA), 2014 IEEE International Conference on*, (May 2014), pp. 4881–4886.

[20] M. Ding and A. Fenster, A real-time biopsy needle segmentation technique using Hough transform., *Medical Physics* **30**(8) (2003) 2222 – 2233.

[21] S. Okazawa, R. Ebrahimi, J. Chuang, R. Rohling and S. Salcudean, Methods for segmenting curved needles in ultrasound images., *Medical Image Analysis* **10**(3) (2006) 330 – 342.

[22] M. Waine, C. Rossa, R. Sloboda, N. Usmani and M. Tavakoli, Three-dimensional needle shape estimation in trus-guided prostate brachytherapy using 2-d ultrasound images, *IEEE Journal of Biomedical and Health Informatics* **20** (Nov 2016) 1621–1631.

[23] M. Khadem, C. Rossa, N. Usmani, R. S. Sloboda and M. Tavakoli, Semi-automated needle steering in biological tissue using an ultrasound-based deflection predictor, *Annals of Biomedical Engineering* **45**(4) (2017) 924–938.

[24] B. Fallahi, C. Rossa, R. S. Sloboda, N. Usmani and M. Tavakoli, Sliding-based image-guided 3D needle steering in soft tissue, *Control Engineering Practice* **63** (2017) 34 – 43.

[25] J. Carriere, C. Rossa, R. Sloboda, N. Usmani and M. Tavakoli, Real-time needle shape prediction in soft-tissue based on image segmentation and particle filtering, *2016 IEEE International Conference on Advanced Intelligent Mechatronics (AIM)*, (July 2016), pp. 1204–1209.

[26] V. Kallem and N. Cowan, Image guidance of flexible tip-steerable needles, *Robotics, IEEE Transactions on* **25** (Feb 2009) 191–196.

[27] D. Ashlock, *Evolutionary Computation for Modeling and Optimization* (Springer, New York, 2010).

[28] R. Richa, R. Sznitman, R. Taylor and G. Hager, Visual tracking using the sum of conditional variance, *2011 IEEE/RSJ International Conference on Intelligent Robots and Systems*, (Sept 2011), pp. 2953–2958.

[29] B. D. Lucas and T. Kanade, An iterative image registration technique with an application to stereo vision, *Proceedings of the 7th International Joint Conference on Artificial Intelligence - Volume 2, IJCAI'81*, (Morgan Kaufmann Publishers Inc., San Francisco, CA, USA, 1981), pp. 674–679.

Jay Carriere earned his B.Sc. in Electrical Engineering from the University of Alberta, Alberta, Canada in 2011. He is currently pursuing a Ph.D. in the Electrical and Computer Engineering Department at the University of Alberta and is working on ultrasound image processing and ultrasound image guided control of needle deflection for prostate brachytherapy.

Mohsen Khadem received his B.Sc. and M.Sc. degrees in mechanical engineering from Shiraz University and Sharif University of Technology, in 2010 and 2013, respectively. He received the Ph.D degree in electrical and computer engineering from the University of Alberta, Canada, in 2017. He is currently a Post-Doctoral Research Fellow with the Department of Medical Physics and Biomedical Engineering, University College London. His current research interests include medical robotics, image-guided surgery, and continuum robots.

Carlos Rossa is an Assistant Professor of Mechatronics in the Faculty of Engineering and Applied Science at the Univerity of Ontario Institute of Technology, Oshawa, ON, Canada. He received his BEng and MSc degrees in Mechanical Engineering from the Ecole Nationale d'Ingénieurs de Metz, Metz, France, both in 2010, and earned his PhD degree in Mechatronics and Robotics from the Université Pierre et Marie Curie, Paris, France, in 2013, under the auspices of the French Atomic Energy Commission (CEA). From 2014 to 2017, he was a post-doctoral fellow at the University of Alberta, Edmonton, Canada. His research interests include medical robotics, haptics, and mechatronics.


Nawaid Usmani received his M.D. from McMaster University in 2001. He is currently an Assistant Professor in the Department of Oncology at the University of Alberta. His main focus on research is in prostate brachytherapy. Currently, prostate brachytherapy is an increasingly popular treatment option for localized prostate cancer due to its excellent efficacy, good toxicity profile and convenience. However, there remains a great deal of potential to improve the current technique. Dr. Usmani's main objective for this research is to characterize current brachytherapy techniques and identify strategies for improving this treatment. This includes quantifying inaccuracies in current brachytherapy techniques, identifying patient populations at a higher risk of toxicity from this treatment, and finding ways to improve our outcomes with brachytherapy implants (using technical and translational approaches).


Ronald Sloboda received his Ph.D. in Nuclear Physics from the University of Alberta in 1979. He is currently a Professor in the Department of Oncology at the University of Alberta. His main research interests are dosimetry and treatment planning for brachytherapy, including the design of clinical studies to obtain patient data that inform model-based dose calculation. His current work is focused on incorporating MRI in the treatment planning, delivery and evaluation processes, particularly for permanent prostate implants and intracavitary cervix treatments.


Mahdi Tavakoli is a Professor in the Department of Electrical and Computer Engineering, University of Alberta, Canada. He received his BSc and MSc degrees in Electrical Engineering from Ferdowsi University and K.N. Toosi University, Iran, in 1996 and 1999, respectively. He received his PhD degree in Electrical and Computer Engineering from the University of Western Ontario, Canada, in 2005. In 2006, he was a post-doctoral researcher at Canadian Surgical Technologies and Advanced Robotics (CSTAR), Canada. In 2007-2008, he was an NSERC Post-Doctoral Fellow at Harvard University, USA. Dr. Tavakoli's research interests broadly involve the areas of robotics and systems control. Specifically, his research focuses on haptics and teleoperation control, medical robotics, and image-guided surgery. Dr. Tavakoli is the lead author of Haptics for Teleoperated Surgical Robotic Systems (World Scientific, 2008). He is an Associate Editor for IEEE/ASME Transactions on Mechatronics, Journal of Medical Robotics Research, Control Engineering Practice, and Mechatronics.